‡ Present address: Stanford Institute for Materials and Energy Sciences, SLAC National Accelerator Laboratory and Stanford University, 2575 Sand Hill Road, Menlo Park, CA 94025, USA.
§ Present address: Department of Physics, Faculty of Sciences, University of Balamand, PO Box 100, Tripoli, Lebanon.
¶ Present address: Dipartimento di Fisica, Politecnico di Milano, Piazza Leonardo da Vinci 32, I-20133 Milano, Italy.
‡‡ Present address: Karlsruhe Institut für Technologie, Institut für Festkörperphysik, Hermann-v.-Helmholtz-Platz 1, D-76344 Eggenstein-Leopoldshafen, Germany.
§§ Present address: MAX IV Laboratory, Lund University, SE-221 00 Lund, Sweden.
¶¶ Present address: Dipartimento di Fisica, Università di Trento, via Sommarive 14, I-38123 Povo (TN), Italy.
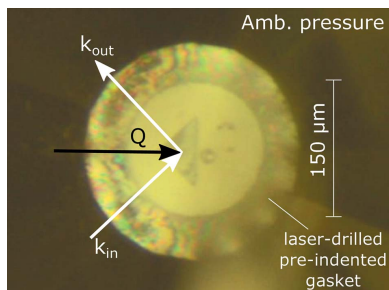
Resonant inelastic X-ray scattering of magnetic excitations under pressure

Matteo Rossi,[a]*‡ Christian Henriquet,[a] Jeroen Jacobs,[a] Christian Donnerer,[b] Stefano Boseggia,[b,c] Ali Al-Zein,[a]§ Roberto Fumagalli,[a]¶ Yi Yao,[a]‡‡ James G. Vale,[b,d] Emily C. Hunter,[e] Robin S. Perry,[b,e] Innokenty Kantor,[a]§§ Gaston Garbarino,[a] Wilson Crichton,[a] Giulio Monaco,[a]¶¶ Desmond F. McMorrow,[b] Michael Krisch[a] and Marco Moretti Sala[a]¶

[a]ESRF – The European Synchrotron, 71 Avenue des Martyrs, CS 40220, F-38043 Grenoble, France, [b]London Centre for Nanotechnology and Department of Physics and Astronomy, University College London, Gower Street, London WC1E 6BT, UK, [c]Diamond Light Source, Harwell Science and Innovation Campus, Didcot, Oxfordshire OX11 0DE, UK, [d]Laboratory for Quantum Magnetism, Ecole Polytechnique Fédérale de Lausanne (EPFL), CH-1015, Switzerland, and [e]Centre for Science at Extreme Conditions, University of Edinburgh, Mayfield Road, Edinburgh EH9 3JZ, UK. *Correspondence e-mail: rossim@stanford.edu

Resonant inelastic X-ray scattering (RIXS) is an extremely valuable tool for the study of elementary, including magnetic, excitations in matter. The latest developments of this technique have mostly been aimed at improving the energy resolution and performing polarization analysis of the scattered radiation, with a great impact on the interpretation and applicability of RIXS. Instead, this article focuses on the sample environment and presents a setup for high-pressure low-temperature RIXS measurements of low-energy excitations. The feasibility of these experiments is proved by probing the magnetic excitations of the bilayer iridate $Sr_3Ir_2O_7$ at pressures up to 12 GPa.

1. Introduction

Resonant inelastic X-ray scattering (RIXS) is a photon-in–photon-out spectroscopic technique that allows the study of the low-energy physics of materials by probing their elementary excitations (Schülke, 2007; Ament et al., 2011a). The RIXS process consists of the resonant photoexcitation of a core electron into an empty state above the Fermi level and the subsequent radiative de-excitation of the system. The final state of the system – either the ground state itself or an excited state – is characterized by the energy, momentum and polarization difference between the incident and emitted photons. Due to the resonant nature of the scattering process and the use of X-rays, RIXS is an element- and orbital-selective momentum-resolved bulk-sensitive technique (Ament et al., 2011a). Different types of excitations can be accessed over an extended energy range, from several hundreds of electronvolts down to a few millielectronvolts, and this limit is continuously being pushed. Indeed, in the last decade, enormous progress has been made in terms of energy resolution by building RIXS spectrometers on dedicated beamlines (Moretti Sala et al., 2013, 2018; Lai et al., 2014; Dvorak et al., 2016; Kim et al., 2018; Brookes et al., 2018). At the same time, initial difficulties in the interpretation of RIXS experiments have been overcome by exploiting its complementarity to other experimental techniques and developing suitable theories (Ament et al., 2009, 2011a,b; Haverkort, 2010; Moretti Sala et al., 2014). A prominent example of RIXS application originates from the

Amb. pressure

theoretical demonstration (Ament *et al.*, 2009; Haverkort, 2010; Moretti Sala *et al.*, 2011) and experimental observation (Braicovich *et al.*, 2010) that RIXS can detect single spin-flip excitations in copper-based superconductors (cuprates), leading to an extensive use of RIXS for the study of their magnetic dynamics (Le Tacon *et al.*, 2011; Dean *et al.*, 2013, 2015) in a manner that is complementary to inelastic neutron scattering (INS) (Tranquada *et al.*, 1989; Coldea *et al.*, 2001; Headings *et al.*, 2010).

In the hard X-ray energy range, RIXS benefits from an additional advantage: it can be coupled to complex sample environments to study matter under extreme conditions (Rueff & Shukla, 2010; Kim, 2016). In particular, the application of high pressure is a valuable tool to investigate the properties of matter (Mao *et al.*, 2018), since it can effectively alter the electron density and, ultimately, induce structural, electronic and magnetic phase transitions (Klotz, 2012; Gor'kov & Kresin, 2018; Mao *et al.*, 2018). However, high-energy-resolution RIXS measurements at high pressure are difficult (Rueff & Shukla, 2010; Kim, 2016) and even more so when dealing with low-energy excitations, such as magnetic ones. As a matter of fact, to the best of our knowledge, no such measurements have ever been reported. Note that this field is rather unexplored as a whole, as the main probe of magnetic excitations, INS, is limited to relatively low pressures ($\sim$1 GPa) (Klotz, 2012) by the competing constraints on the sample volume imposed by neutron techniques and high-pressure experiments.

We here discuss recent instrumental developments made on beamline ID20 at the ESRF that allowed us to perform RIXS measurements of low-energy magnetic excitations under pressure. As a test case we consider iridium oxides, as they have attracted the attention of the scientific community in the last decade (Witczak-Krempa *et al.*, 2014; Rau *et al.*, 2016). Indeed, they feature electron–electron and spin–orbit interactions of comparable strength, leading to unexpected properties, including the so-called spin–orbit-induced Mott insulating state (Kim *et al.*, 2008, 2009).

The single-layer material Sr_2IrO_4 ($n = 1$) is the prototypical spin–orbit-induced Mott insulator (Kim *et al.*, 2008, 2009) and develops long-range (canted) antiferromagnetic (AFM) order below a Néel temperature of $\sim$240 K (Cao *et al.*, 1998). It has been the focus of numerous theoretical and experimental investigations regarding its similarities with cuprates (Kim *et al.*, 2012a, 2014b, 2015; de la Torre *et al.*, 2015; Yan *et al.*, 2015; Gretarsson *et al.*, 2016; Liu *et al.*, 2016; Terashima *et al.*, 2017; Pincini *et al.*, 2017; Calder *et al.*, 2018) and the possibility of hosting unconventional superconductivity (Wang & Senthil, 2011; Watanabe *et al.*, 2013; Yang *et al.*, 2014; Meng *et al.*, 2014).

The bilayer material $Sr_3Ir_2O_7$ is the $n = 2$ member of the Ruddlesden–Popper series $Sr_{n+1}Ir_nO_{3n+1}$ and shares many physical properties with Sr_2IrO_4, including a Mott-insulating ground state of relativistic nature (Moon *et al.*, 2008) and the tendency to develop long-range AFM order below $\sim$280 K (Cao *et al.*, 2002; Boseggia *et al.*, 2012). However, the microscopic mechanisms that govern magnetism in $Sr_3Ir_2O_7$ are

debated, since two different theoretical models have been proposed to interpret its magnetic structure and dynamics (Kim *et al.*, 2012b; Moretti Sala *et al.*, 2015). The two models are mutually exclusive, as they cast the main exchange couplings into two opposite scenarios: Kim *et al.* proposed a linear spin–wave approach with dominant intralayer interaction (Kim *et al.*, 2012b), whereas Moretti Sala *et al.* pursued a bond-operator mean-field approach with predominant interlayer dimer-like interactions (Moretti Sala *et al.*, 2015). Despite fundamental differences, the two theoretical approaches fit equally well the magnetic dynamics of $Sr_3Ir_2O_7$ at ambient pressure, with a bandwidth of $\sim$70 meV and an anomalously large magnetic gap of $\sim$90 meV. In order to discriminate between the two models, the evolution of magnetic excitations should be tested against well defined and controlled perturbations of the system. In this respect, the magnetic dynamics of $(Sr_{1-x}La_x)_3Ir_2O_7$ were studied as a function of doping (up to $x = 0.1$), but without conclusive evidence in favour of either model (Hogan *et al.*, 2016a; Lu *et al.*, 2017). In addition, it is often argued that doping is not a 'clean' perturbation, as it introduces disorder into the system, thus making the interpretation of experimental results less reliable. We therefore propose to use physical pressure as an alternative and clean method of perturbing the system and prove the feasibility of this approach. Indeed, the application of physical pressure does not modify the chemical composition of the system and can be gradually tuned from arbitrarily small to very large values, up to hundreds of gigapascals.

Thus, once established as a viable technique, it is not difficult to imagine that the use of high-pressure RIXS to probe the magnetic quasiparticle spectrum will find general application and produce results of widespread interest.

2. Background considerations

High-pressure experiments require the use of so-called diamond anvil cells (DACs), in which two diamonds are pushed against one other to apply pressure to a sample in between them. The sample chamber is obtained by perforating a small hole in a gasket that prevents the two diamonds from touching. The high-pressure environment therefore completely embeds the sample and imposes several constraints on the experiment, including the limitation of X-ray experiments under high pressure to the hard X-ray range. RIXS excitations of single-crystalline materials are usually probed at specific transferred momenta, hence the requirement for precise scattering geometries. However, the severe geometric constraints imposed by the DAC and the gasket often limit the accessible scattering geometries.

Another important aspect to take into account is that the sample environment absorbs part of the radiation. Since RIXS is a photon-hungry technique, it is therefore imperative to minimize the X-ray absorption through the sample environment, as well as to maximize the collected solid angle and optimize the sample volume. This last point is very delicate: on the one hand, the maximum reachable pressure depends on the diamond culets, which ultimately limit the sample

dimensions; on the other hand, the sample size should exceed the X-ray penetration depth in order to maximize the RIXS scattering cross section. The best compromise is that the sample has roughly the dimensions of the X-ray focal spot size ($\sim$20 μm × 10 μm) times the X-ray penetration depth ($\sim$8 μm in $Sr_3Ir_2O_7$ at the Ir L_3 edge).

Finally, X-ray scattering from the sample environment – typically non-resonant elastic and inelastic scattering from the gasket and/or the diamonds of the DAC – contributes to the background noise, which may even be stronger than the actual RIXS signal. Note that elastically scattered X-rays from a source slightly off the sample position will impinge on the crystal analyser at an angle different from the nominal Bragg angle and will be interpreted as inelastic signal, thus potentially giving rise to artifacts in the RIXS spectrum. In addition, X-ray scattering from crystalline diamonds will feature sharp phonon peaks at an energy loss of up to $\sim$170 meV (Warren *et al.*, 1967). Similarly, the gasket is also a source of inelastic scattering. If amorphous beryllium is used, however, the phonon signal is a broad weak distribution, resembling the phonon density of states and extending up to $\sim$100 meV (Schmunk *et al.*, 1962; Stedman *et al.*, 1976).

In order to cope with most of the difficulties described above, we have adopted a scattering geometry as close as possible to 90° where the X-rays travel through the gasket of the DAC. For the horizontally polarized light used in our experiments, this geometry leads to a large suppression of all spurious processes arising from Thomson scattering. The choice of the gasket material is then restricted to beryllium, because of its low absorption of hard X-rays. The main drawbacks are its low shear strength and brittleness, which limit the maximum reachable pressure.

3. Sample environment

3.1. DAC and gasket

DACs are standard tools to perform experiments at pressures up to several hundreds of gigapascals (Jayaraman, 1983; Bassett, 2009). For our experiment we designed and built a customized panoramic DAC, shown in Fig. 1: it features two large opening windows of 140° in the scattering plane and 80° in the plane orthogonal to it [see also Sahle *et al.* (2017)].
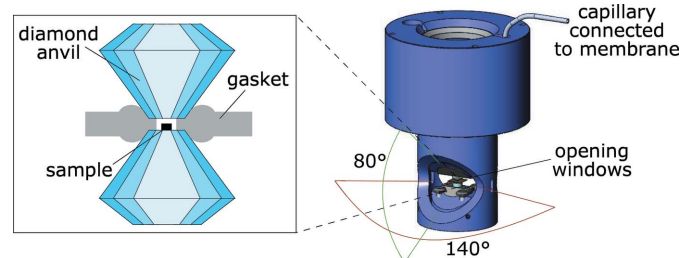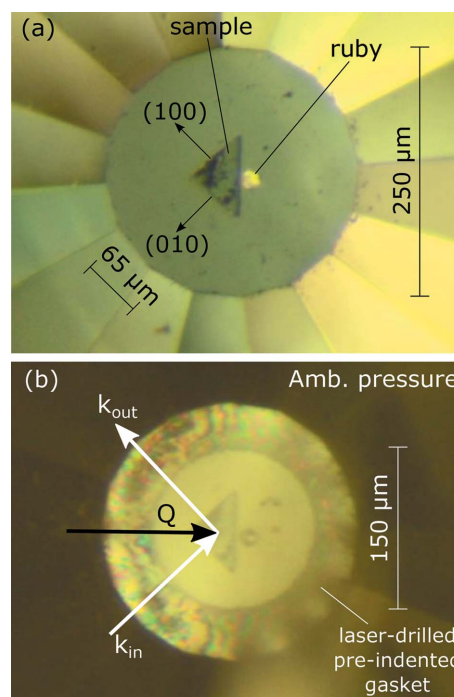

Figure 1
The panoramic diamond anvil cell used for high-pressure RIXS experiments. The two diamonds are in the middle of the opening window. The compression axis is vertical and the scattering plane is horizontal in the figure reference frame.

The extra-high 16-sided (100)-oriented diamond anvils are in the middle of the opening window. They are based on the type Ia Boehler–Almax design (Boehler & Hantsetters, 2004) (diameter 3.1 mm, height 2.72 mm, angle of the diamond faces 25°). Diamonds of culet size ranging from 0.25 mm (maximum pressure $\sim$80 GPa) to 0.5 mm (maximum pressure $\sim$30 GPa) are used to cover different pressure ranges. A cylinder-piston system (modified Letoullec design; Letoullec *et al.*, 1988) allows the movement of the diamond anvils along the compression axis. The anvils are pushed together by the application of force on one diamond through a gas-driven membrane that is connected to a pressure controller. The beryllium gasket, with an outer diameter of 5 mm and a thickness of 0.2 mm, was pre-indented to approximately 1/10 of the culet size (*i.e.* $\sim$30–50 μm) before the experiment and a sample chamber with a diameter approximately equal to 50–60% of the culet size is laser-drilled in the centre to accommodate the sample.

An image of a typical sample loading is shown in Fig. 2. Panel (*a*) shows the culet of one anvil, in the middle of which a single crystal of $Sr_3Ir_2O_7$ is loaded. The sample has been polished roughly to the desired size. $Sr_3Ir_2O_7$ naturally cleaves into layers orthogonal to the *c* axis, with sharp edges parallel either to the (100) or (110) axes, as illustrated in Fig. 2. We chose inert neon as the pressure-transmitting medium since it is almost transparent to X-rays and it ensures a quasi-hydrostatic compression of the sample. The pressure within the DAC was determined by tracking the energy position of the R_1
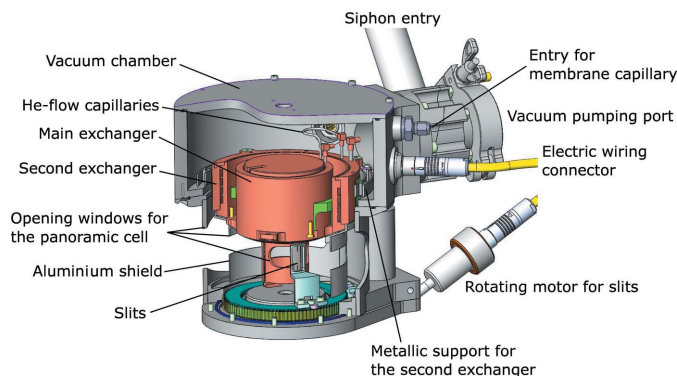

Figure 2
(*a*) The $Sr_3Ir_2O_7$ single crystal and ruby sphere loaded at the centre of the culet with a diameter of 250 μm. The sample has a triangular shape with edges of $\sim$65 μm parallel to the high-symmetry directions of the lattice. (*b*) The $Sr_3Ir_2O_7$ and ruby sphere after the pre-indented laser-drilled gasket has been placed between the diamond anvils. A sketch of the experimental geometry is also shown.

fluorescence line of a ruby (Al_2O_3:Cr^{3+}) sphere placed next to the sample (Mao & Bell, 1976). Fig. 2(b) shows the sample and the ruby sphere after the gasket has been put between the diamond anvils. The laser-drilled sample chamber with a diameter of 150 µm is visible.

3.2. Cryostat

The panoramic DAC is placed inside a cryostat in such a way that the compression axis is vertical and the wide opening windows are horizontal in the laboratory reference frame (Fig. 3). The outer part of the cryostat is the vacuum chamber. It is made of stainless steel to withstand ambient pressure and is fixed on the RIXS sample goniometer. Two large windows have been opened in the walls of the chamber and covered by an X-ray-transparent 0.1 mm-thick Kapton foil. The vacuum is as good as $\leq 10^{-7}$ mbar during the measurements (1 bar = 100 000 Pa). The vacuum chamber hosts the entries for the siphon, the vacuum pumping port, the electric wiring connectors and a feed-through for the capillary that connects the pressure controller to the cell membrane. The panoramic DAC is placed inside a copper main heat exchanger, which is cooled down by a continuous flow of helium. Its temperature is measured by a Cernox sensor and regulated by resistive Kapton foil heaters. Helium then flows through stainless steel capillaries into a copper secondary heat exchanger before it is evacuated through the input siphon. The temperature of the secondary exchanger is measured and regulated in a similar fashion to the main heat exchanger. It is designed such that the contact surface between the secondary exchanger and the vacuum chamber is minimized and the thermal paths are maximized for thermal decoupling. Furthermore, thermally insulating washers are utilized to fix the two elements. Because of the cylindrically symmetric design of the cryostat, the position of the DAC moves by less than ∼40 µm in the horizontal plane and by ∼160 µm along the vertical axis when cooled from room temperature to 100 K.

A system of motorized slits is placed inside the cryostat chamber. The slits rotate around the DAC compression axis at a distance of 16.5 mm from the sample. The slit aperture defines the region around the sample that is seen by the spectrometer, therefore their use allows the removal of most of the background coming from the sample environment (Yoshida et al., 2014). The effect of the slit is clear upon inspection of Fig. 4, which shows RIXS spectra of $Sr_3Ir_2O_7$ measured with (filled circles) and without (empty squares) slits. The background due to the sample environment extends up to energy losses of ∼0.3 eV and almost covers the magnetic signal at ∼0.1 eV. The use of slits suppresses most of the background and allows the safe recovery of the magnetic signal from the sample. Three slit apertures are available: 0.08, 0.16 and 0.32 mm. The field of view of the spectrometer is 0.2, 0.28 and 0.45 mm in the three cases, respectively, considering a mask of 15 mm placed in front of the crystal analyser. The field of view is related to the diamond culet size and sample dimensions and eventually to the pressure range of interest. Hence, the smallest slit aperture is used when pressures in the ∼10 GPa range are targeted, while larger apertures are used for pressures in the megapascal to ∼1 GPa regime. In this work, all spectra are collected with the smallest slit aperture.

4. RIXS measurements

Iridium L_3 edge (∼11.22 keV) RIXS measurements were performed on beamline ID20 at the ESRF. The beamline was designed and constructed within the framework of the recent ESRF Upgrade – Phase I. It is a flagship beamline for resonant and non-resonant inelastic hard X-ray scattering spectroscopy (Moretti Sala et al., 2018; Huotari et al., 2017). It has been conceived to maximize the photon flux at the sample position, cover a wide energy range (4–20 keV), optimize the energy resolution and guarantee a small stable beam over a long interval of time. These are essential requirements for RIXS experiments, in particular under extreme conditions. During the measurements, the incoming X-rays were monochromated to 11.2165 keV by the joint use of an Si(111) double-crystal monochromator and a backscattering Si(844) post monochromator. A Kirkpatrick–Baez (KB) mirror system focused the incoming beam to a spot size smaller than 10 µm × 20 µm (vertical × horizontal). The X-rays scattered by the sample were energy-analysed by a Rowland-circle-based spectrometer, equipped with a spherical Si(844) diced crystal analyser and a position-sensitive detector. The overall energy resolu-
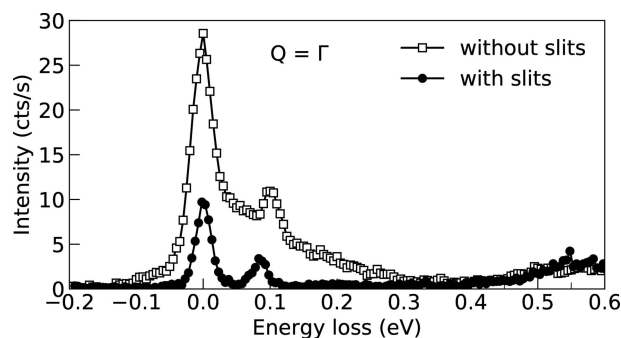

Figure 3
The helium-flow cryostat for high-pressure low-temperature RIXS experiments. The panoramic DAC is lodged inside the main heat exchanger.

Figure 4
RIXS spectra for $Sr_3Ir_2O_7$ collected at equivalent Γ points with (filled circles) and without (empty squares) slits. Spectra are plotted in counts per second.

tion is as good as 25 meV and the incident photon flux is $\sim 10^{12}$ photons s^{-1} at the sample position (Moretti Sala *et al.*, 2013, 2018). Further information about the RIXS spectrometer of beamline ID20 can be found in the work of Moretti Sala *et al.* (2018).

A sketch of the scattering geometry employed during the measurements is shown in Fig. 2(*b*). The incoming and outgoing photon wavevectors are $\mathbf{k}_{in}$ and $\mathbf{k}_{out}$, respectively, while $\mathbf{Q} = \mathbf{k}_{in} - \mathbf{k}_{out}$ is the momentum transfer. Note that this geometry allows us to reach the boundary (π, π) of the two-dimensional Brillouin zone.

5. Results and discussion

The setup described above has been employed to determine the pressure dependence of the magnetic structure and dynamics of $Sr_3Ir_2O_7$. Fig. 5(*a*) displays overview raw RIXS spectra for $Sr_3Ir_2O_7$ measured at momentum transfer $\mathbf{Q}$ = (3.5, 3.5, 0) reciprocal-lattice units (r.l.u.) corresponding to the two-dimensional Brillouin zone boundary (π, π). The spectra are normalized to the features above 0.4 eV. As can be seen, both spectra measured at ambient pressure (black circles) and at P = 3.1 GPa (red diamonds) are qualitatively similar: besides the elastic line, both spectra feature a sharp (FWHM $\simeq$ 0.04 eV) peak at $\sim$0.1 eV and a broad (FWHM $\simeq$ 0.45 eV) excitation centred at $\sim$0.75 eV. The first feature is ascribed to the single magnon excitation (Kim *et al.*, 2012*b*; Moretti Sala *et al.*, 2015), while the second is ascribed to the transition of a hole from the $j_{eff} = 1/2$ ground state to the $j_{eff} = 3/2$ band, in agreement with previous work on the sister compound Sr_2IrO_4 (Kim *et al.*, 2012*a*, 2014*a*). The pressure dependence of the latter excitation at room temperature has already been investigated by Ding and co-workers, who have found that the peak position changes by at most $\sim$15% from ambient pressure to approximately 65 GPa, while the width does not undergo a significant change (Ding *et al.*, 2016). We note that magnetic excitations could not be resolved in the RIXS spectra measured by Ding *et al.* (2016), not only because the measurements were carried out at room temperature, but also because of the spurious signal from the sample environment extending up to several hundreds of millielectronvolts. In contrast, the magnetic excitations are clearly distinguished in our spectra, as highlighted in Figs. 5(*b*) and 5(*c*), and show an unambiguous softening when the pressure is increased up to 12 GPa. In Figs. 5(*b*) and 5(*c*), the spectra are plotted in counts per second (cts s^{-1}) and the spectrum collected at ambient pressure is multiplied by a factor for better comparison. We observe that the intensity drops by a factor of $\sim$4–7 when the high-pressure sample environment is employed.

Before discussing the implications of the magnetic mode softening, we briefly address the pressure dependence of the magnetic structure of $Sr_3Ir_2O_7$. Magnetic diffraction peaks are shown in Fig. 6 up to 12 GPa. The spectra were collected by monitoring the elastic signal while scanning along the high-symmetry lines of the reciprocal lattice parallel to the (100) and (001) directions [Figs. 6(*a*) and 6(*b*), respectively]. As can be seen, the magnetic diffraction peaks are broadened and
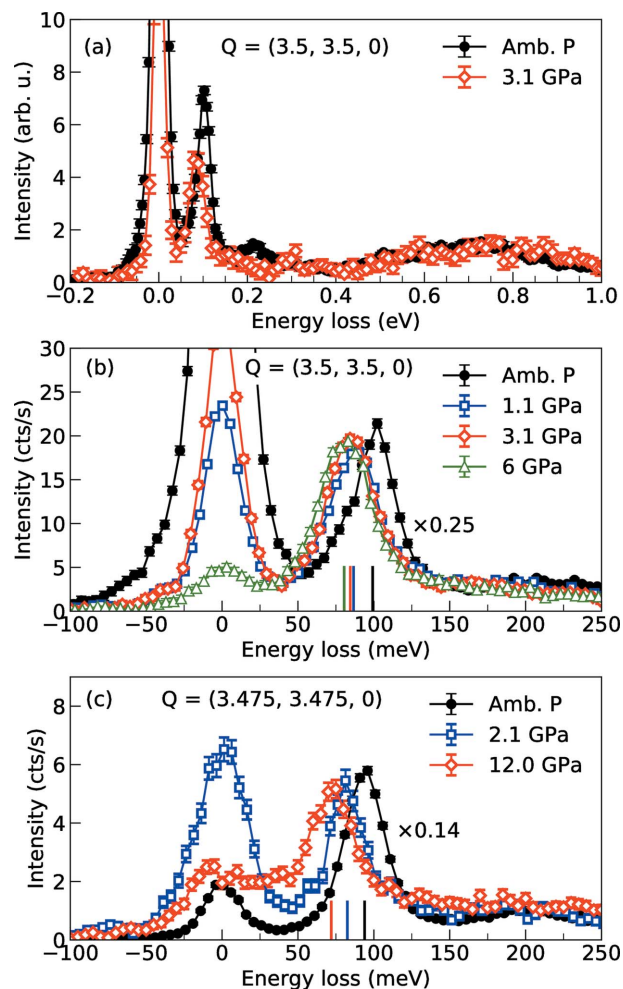
Figure 5
(*a*) Iridium L_3 edge RIXS spectra of $Sr_3Ir_2O_7$ measured at ambient pressure (black circles) and at P = 3.1 GPa (red diamonds). The spectra were collected at T = 150 K and $\mathbf{Q}$ = (3.5, 3.5, 0) r.l.u. and are normalized to the orbital excitations above 0.4 eV. (*b*) The magnetic regions of the RIXS spectra measured at T = 150 K and $\mathbf{Q}$ = (3.5, 3.5, 0) r.l.u., showing the softening of the magnetic mode with pressure. (*c*) The magnetic regions of the RIXS spectra measured at T = 100 K and $\mathbf{Q}$ = (3.475, 3.475, 0) r.l.u. The spectra acquired at ambient pressure in panels (*b*) and (*c*) are multiplied by 0.25 and 0.14, respectively, in order to compare them with the high-pressure RIXS data.

damped with pressure, but overall the long-range AFM order survives at least until 12 GPa. Above this pressure, we noticed a degradation of the sample quality, as testified by a drastic broadening and suppression of the charge diffraction peaks. Therefore, the results can be safely discussed only up to 12 GPa.

Having established that the underlying magnetic structure is preserved, we now discuss the pressure evolution of the magnetic mode. This is summarized in Fig. 7, which displays the pressure dependence of the magnon peak position (black circles and squares) together with a linear fit (red solid line) to the experimental data points. The softening rate is $\sim$1.5 meV GPa^{-1}. A linear extrapolation of the data points to higher pressures (dashed line) hints at a collapse of the magnetic mode around $\sim$55–60 GPa. We note that a structural phase transition has been reported in $Sr_3Ir_2O_7$ at 54 GPa
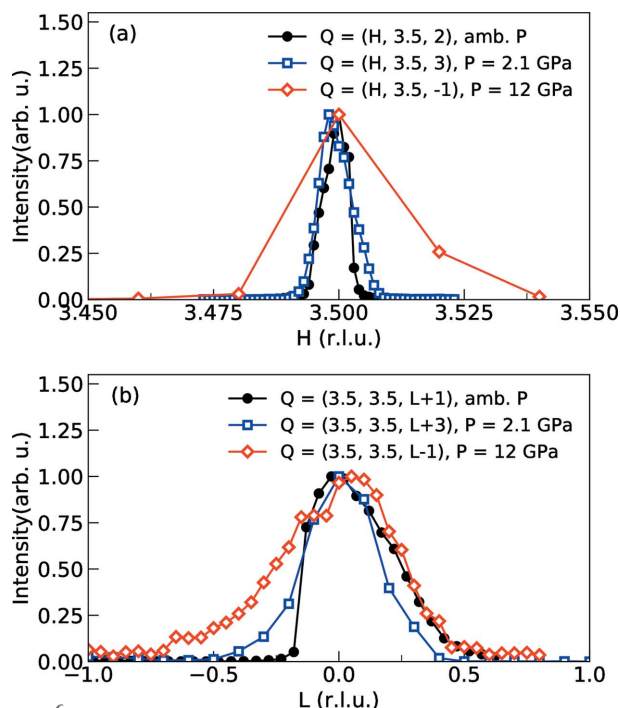
Figure 6
The pressure dependence of the magnetic diffraction peaks of $Sr_3Ir_2O_7$ measured by collecting the elastic signal while scanning along the high-symmetry directions of the reciprocal lattice parallel to (a) the (100) axis and (b) the (001) axis. The scans were collected at $T = 100$ K.

(Donnerer *et al.*, 2016), therefore suggesting a strong link between magnetic and lattice degrees of freedom, possibly resulting from the strong spin–orbit coupling.

In relation to the debate about the most suitable theoretical model to describe the magnetic dynamics of $Sr_3Ir_2O_7$, we recall that high-pressure diffraction measurements revealed a higher compressibility of the *a* and *b* axes with respect to the *c* axis (Donnerer *et al.*, 2016). Indeed, applied pressure is mostly accommodated by rotating the IrO_6 octahedra around the *c* axis, thus causing the in-plane Ir—O—Ir bond angle to deviate further from the straight (180°) geometry. Along the *c* axis, instead, the Ir—O—Ir bond angle is unchanged, while the Ir—O—Ir bond length is shortened (Donnerer *et al.*, 2016; Ding
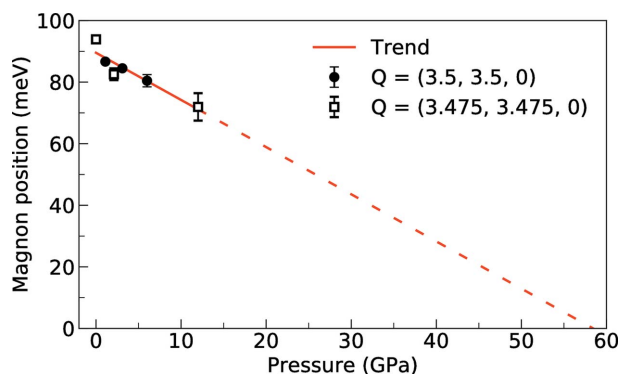
Figure 7
The energy positions of the magnon peak (black circles and squares), with the solid red line resulting from the fit of the data and the dashed red line from linear extrapolation of the pressure evolution of the magnon softening until the collapse of the magnetic gap, which is estimated to occur at a pressure of ∼58 GPa.

et al., 2016). Since electronic interactions are strongly affected by bond geometry (Jackeli & Khaliullin, 2009), the pressure dependence of the dominant magnetic couplings can be guessed. In particular, the intralayer exchange coupling is expected to decrease with pressure, while the interlayer exchange coupling should be less affected by pressure and, if anything, is expected to increase. In the light of these expectations, we speculate that it is easier to reconcile our experimental results with the linear spin–wave theory approach (Kim *et al.*, 2012b), because the magnetic gap in the quantum dimer model should scale with the interlayer exchange coupling to first order (Moretti Sala *et al.*, 2015). Our qualitative discussion is also consistent with a recent refinement of the crystal structure of $Sr_3Ir_2O_7$, since the departure from the pure tetragonal lattice is found to be very small (Hogan *et al.*, 2016b). A comprehensive interpretation of the experimental results goes well beyond the scope of the present paper, which is more to establish the general feasibility of performing high-pressure RIXS experiments of magnetic excitations and provide the scientific community with an additional tool to study electronic and magnetic dynamics in matter under extreme conditions.

6. Conclusions and outlook

To summarize, we have described recent instrumental upgrades carried out on beamline ID20 at the ESRF that allowed us to perform RIXS measurements of magnetic excitations at high pressure. In particular, we have measured the magnetic excitations of the bilayer perovskite $Sr_3Ir_2O_7$ up to 12 GPa and observed a softening of the magnetic mode with pressure at a rate of ∼1.5 meV GPa^{-1}. Extrapolation of this behaviour to higher pressures shows that the collapse of the magnetic gap might be concomitant with the structural phase transition reported at 54 GPa (Donnerer *et al.*, 2016), suggesting a strong link between magnetic and lattice degrees of freedom. Most importantly, we have demonstrated the feasibility of RIXS experiments of low-energy excitations under extreme conditions of temperature and pressure.

References

Ament, L. J. P., Ghiringhelli, G., Sala, M. M., Braicovich, L. & van den Brink, J. (2009). *Phys. Rev. Lett.* **103**, 117003.
Ament, L. J. P., Khaliullin, G. & van den Brink, J. (2011b). *Phys. Rev. B*, **84**, 020403.

Ament, L. J. P., van Veenendaal, M., Devereaux, T. P., Hill, J. P. & van den Brink, J. (2011*a*). *Rev. Mod. Phys.* **83**, 705–767.

Bassett, W. A. (2009). *High. Press. Res.* **29**, 163–186.

Boehler, R. & De Hantsetters, K. (2004). *High. Press. Res.* **24**, 391–396.

Boseggia, S., Springell, R., Walker, H. C., Boothroyd, A. T., Prabhakaran, D., Wermeille, D., Bouchenoire, L., Collins, S. P. & McMorrow, D. F. (2012). *Phys. Rev. B*, **85**, 184432.

Braicovich, L., van den Brink, J., Bisogni, V., Sala, M. M., Ament, L. J. P., Brookes, N. B., De Luca, G. M., Salluzzo, M., Schmitt, T., Strocov, V. N. & Ghiringhelli, G. (2010). *Phys. Rev. Lett.* **104**, 077002.

Brookes, N., Yakhou-Harris, F., Kummer, K., Fondacaro, A., Cezar, J., Betto, D., Velez-Fort, E., Amorese, A., Ghiringhelli, G., Braicovich, L., Barrett, R., Berruyer, G., Cianciosi, F., Eybert, L., Marion, P., van der Linden, P. & Zhang, L. (2018). *Nucl. Instrum. Methods Phys. Res. A*, **903**, 175–192.

Calder, S., Pajerowski, D. M., Stone, M. B. & May, A. F. (2018). *Phys. Rev. B*, **98**, 220402.

Cao, G., Bolivar, J., McCall, S., Crow, J. E. & Guertin, R. P. (1998). *Phys. Rev. B*, **57**, R11039–R11042.

Cao, G., Xin, Y., Alexander, C. S., Crow, J. E., Schlottmann, P., Crawford, M. K., Harlow, R. L. & Marshall, W. (2002). *Phys. Rev. B*, **66**, 214412.

Coldea, R., Hayden, S. M., Aeppli, G., Perring, T. G., Frost, C. D., Mason, T. E., Cheong, S.-W. & Fisk, Z. (2001). *Phys. Rev. Lett.* **86**, 5377–5380.

Dean, M. (2015). *J. Magn. Magn. Mater.* **376**, 3–13.

Dean, M. P. M., Dellea, G., Springell, R. S., Yakhou-Harris, F., Kummer, K., Brookes, N. B., Liu, X., Sun, Y.-J., Strle, J., Schmitt, T., Braicovich, L., Ghiringhelli, G., Božović, I. & Hill, J. P. (2013). *Nat. Mater.* **12**, 1019–1023.

Ding, Y., Yang, L., Chen, C.-C., Kim, H.-S., Han, M. J., Luo, W., Feng, Z., Upton, M., Casa, D., Kim, J., Gog, T., Zeng, Z., Cao, G., Mao, H. & van Veenendaal, M. (2016). *Phys. Rev. Lett.* **116**, 216402.

Donnerer, C., Feng, Z., Vale, J. G., Andreev, S. N., Solovyev, I. V., Hunter, E. C., Hanfland, M., Perry, R. S., Rønnow, H. M., McMahon, M. I., Mazurenko, V. V. & McMorrow, D. F. (2016). *Phys. Rev. B*, **93**, 174118.

Dvorak, J., Jarrige, I., Bisogni, V., Coburn, S. & Leonhardt, W. (2016). *Rev. Sci. Instrum.* **87**, 115109.

Gor'kov, L. P. & Kresin, V. Z. (2018). *Rev. Mod. Phys.* **90**, 011001.

Gretarsson, H., Sung, N. H., Porras, J., Bertinshaw, J., Dietl, C., Bruin, J. A. N., Bangura, A. F., Kim, Y. K., Dinnebier, R., Kim, J., Al-Zein, A., Moretti Sala, M., Krisch, M., Le Tacon, M., Keimer, B. & Kim, B. J. (2016). *Phys. Rev. Lett.* **117**, 107001.

Haverkort, M. W. (2010). *Phys. Rev. Lett.* **105**, 167404.

Headings, N. S., Hayden, S. M., Coldea, R. & Perring, T. G. (2010). *Phys. Rev. Lett.* **105**, 247001.

Hogan, T., Bjaalie, L., Zhao, L., Belvin, C., Wang, X., Van de Walle, C. G., Hsieh, D. & Wilson, S. D. (2016*b*). *Phys. Rev. B*, **93**, 134110.

Hogan, T., Dally, R., Upton, M., Clancy, J. P., Finkelstein, K., Kim, Y.-J., Graf, M. J. & Wilson, S. D. (2016*a*). *Phys. Rev. B*, **94**, 100401.

Huotari, S., Sahle, C. J., Henriquet, C., Al-Zein, A., Martel, K., Simonelli, L., Verbeni, R., Gonzalez, H., Lagier, M.-C., Ponchut, C., Moretti Sala, M., Krisch, M. & Monaco, G. (2017). *J. Synchrotron Rad.* **24**, 521–530.

Jackeli, G. & Khaliullin, G. (2009). *Phys. Rev. Lett.* **102**, 017205.

Jayaraman, A. (1983). *Rev. Mod. Phys.* **55**, 65–108.

Kim, B. J., Jin, H., Moon, S. J., Kim, J.-Y., Park, B.-G., Leem, C. S., Yu, J., Noh, T. W., Kim, C., Oh, S.-J., Park, J.-H., Durairaj, V., Cao, G. & Rotenberg, E. (2008). *Phys. Rev. Lett.* **101**, 076402.

Kim, B. J., Ohsumi, H., Komesu, T., Sakai, S., Morita, T., Takagi, H. & Arima, T. (2009). *Science*, **323**, 1329–1332.

Kim, J. (2016). *High. Press. Res.* **36**, 391–403.

Kim, J., Casa, D., Said, A., Krakora, R., Kim, B. J., Kasman, E., Huang, X. & Gog, T. (2018). *Sci. Rep.* **8**, 1958.

Kim, J., Casa, D., Upton, M. H., Gog, T., Kim, Y.-J., Mitchell, J. F., van Veenendaal, M., Daghofer, M., van den Brink, J., Khaliullin, G. & Kim, B. J. (2012*a*). *Phys. Rev. Lett.* **108**, 177003.

Kim, J., Daghofer, M., Said, A. H., Gog, T., van den Brink, J., Khaliullin, G. & Kim, B. J. (2014*a*). *Nat. Commun.* **5**, 4453.

Kim, J., Said, A. H., Casa, D., Upton, M. H., Gog, T., Daghofer, M., Jackeli, G., van den Brink, J., Khaliullin, G. & Kim, B. J. (2012*b*). *Phys. Rev. Lett.* **109**, 157402.

Kim, Y. K., Krupin, O., Denlinger, J. D., Bostwick, A., Rotenberg, E., Zhao, Q., Mitchell, J. F., Allen, J. W. & Kim, B. J. (2014*b*). *Science*, **345**, 187–190.

Kim, Y. K., Sung, N. H., Denlinger, J. D. & Kim, B. J. (2015). *Nat. Phys.* **12**, 1–6.

Klotz, S. (2012). *Techniques in High Pressure Neutron Scattering.* Boca Raton: CRC Press.

Lai, C. H., Fung, H. S., Wu, W. B., Huang, H. Y., Fu, H. W., Lin, S. W., Huang, S. W., Chiu, C. C., Wang, D. J., Huang, L. J., Tseng, T. C., Chung, S. C., Chen, C. T. & Huang, D. J. (2014). *J. Synchrotron Rad.* **21**, 325–332.

Le Tacon, M., Ghiringhelli, G., Chaloupka, J., Sala, M. M., Hinkov, V., Haverkort, M. W., Minola, M., Bakr, M., Zhou, K. J., Blanco-Canosa, S., Monney, C., Song, Y. T., Sun, G. L., Lin, C. T., De Luca, G. M., Salluzzo, M., Khaliullin, G., Schmitt, T., Braicovich, L. & Keimer, B. (2011). *Nat. Phys.* **7**, 725–730.

Letoullec, R., Pinceaux, J. P. & Loubeyre, P. (1988). *High. Press. Res.* **1**, 77–90.

Liu, X., Dean, M. P. M., Meng, Z. Y., Upton, M. H., Qi, T., Gog, T., Cao, Y., Lin, J. Q., Meyers, D., Ding, H., Cao, G. & Hill, J. P. (2016). *Phys. Rev. B*, **93**, 241102.

Lu, X., McNally, D. E., Moretti Sala, M., Terzic, J., Upton, M. H., Casa, D., Ingold, G., Cao, G. & Schmitt, T. (2017). *Phys. Rev. Lett.* **118**, 027202.

Mao, H. K. & Bell, P. M. (1976). *Science*, **191**, 851–852.

Mao, H.-K., Chen, X.-J., Ding, Y., Li, B. & Wang, L. (2018). *Rev. Mod. Phys.* **90**, 015007.

Meng, Z. Y., Kim, Y. B. & Kee, H.-Y. (2014). *Phys. Rev. Lett.* **113**, 177003.

Moon, S. J., Jin, H., Kim, K. W., Choi, W. S., Lee, Y. S., Yu, J., Cao, G., Sumi, A., Funakubo, H., Bernhard, C. & Noh, T. W. (2008). *Phys. Rev. Lett.* **101**, 226402.

Moretti Sala, M., Bisogni, V., Aruta, C., Balestrino, G., Berger, H., Brookes, N. B., Luca, G. M., Di Castro, D., Grioni, M., Guarise, M., Medaglia, P. G., Miletto Granozio, F., Minola, M., Perna, P., Radovic, M., Salluzzo, M., Schmitt, T., Zhou, K. J., Braicovich, L. & Ghiringhelli, G. (2011). *New J. Phys.* **13**, 043026.

Moretti Sala, M., Boseggia, S., McMorrow, D. F. & Monaco, G. (2014). *Phys. Rev. Lett.* **112**, 026403.

Moretti Sala, M., Henriquet, C., Simonelli, L., Verbeni, R. & Monaco, G. (2013). *J. Electron Spectrosc. Relat. Phenom.* **188**, 150–154.

Moretti Sala, M., Martel, K., Henriquet, C., Al Zein, A., Simonelli, L., Sahle, C., Gonzalez, H., Lagier, M.-C., Ponchut, C., Huotari, S., Verbeni, R., Krisch, M. & Monaco, G. (2018). *J. Synchrotron Rad.* **25**, 580–591.

Moretti Sala, M., Schnells, V., Boseggia, S., Simonelli, L., Al-Zein, A., Vale, J. G., Paolasini, L., Hunter, E. C., Perry, R. S., Prabhakaran, D., Boothroyd, A. T., Krisch, M., Monaco, G., Rønnow, H. M., McMorrow, D. F. & Mila, F. (2015). *Phys. Rev. B*, **92**, 024405.

Pincini, D., Vale, J. G., Donnerer, C., de la Torre, A., Hunter, E. C., Perry, R., Moretti Sala, M., Baumberger, F. & McMorrow, D. F. (2017). *Phys. Rev. B*, **96**, 075162.

Rau, J. G., Lee, E. K.-H. & Kee, H.-Y. (2016). *Annu. Rev. Condens. Matter Phys.* **7**, 195–221.

Rueff, J.-P. & Shukla, A. (2010). *Rev. Mod. Phys.* **82**, 847–896.

Sahle, C. J., Rosa, A. D., Rossi, M., Cerantola, V., Spiekermann, G., Petitgirard, S., Jacobs, J., Huotari, S., Moretti Sala, M. & Mirone, A. (2017). *J. Synchrotron Rad.* **24**, 269–275.

Schmunk, R. E., Brugger, R. M., Randolph, P. D. & Strong, K. A. (1962). *Phys. Rev.* **128**, 562–573.

Schülke, W. (2007). *Electron Dynamics by Inelastic X-ray Scattering. Oxford Series on Synchrotron Radiation*, Vol. 7. Oxford University Press.

Stedman, R., Amilius, Z., Pauli, R. & Sundin, O. (1976). *J. Phys. F Met. Phys.* **6**, 157–166.

Terashima, K., Sunagawa, M., Fujiwara, H., Fukura, T., Fujii, M., Okada, K., Horigane, K., Kobayashi, K., Horie, R., Akimitsu, J., Golias, E., Marchenko, D., Varykhalov, A., Saini, N. L., Wakita, T., Muraoka, Y. & Yokoya, T. (2017). *Phys. Rev. B*, **96**, 041106.

Torre, A. de la, McKeown Walker, S., Bruno, F. Y., Riccó, S., Wang, Z., Gutierrez Lezama, I., Scheerer, G., Giriat, G., Jaccard, D., Berthod, C., Kim, T. K., Hoesch, M., Hunter, E. C., Perry, R. S., Tamai, A. & Baumberger, F. (2015). *Phys. Rev. Lett.* **115**, 176402.

Tranquada, J. M., Shirane, G., Keimer, B., Shamoto, S. & Sato, M. (1989). *Phys. Rev. B*, **40**, 4503–4516.

Wang, F. & Senthil, T. (2011). *Phys. Rev. Lett.* **106**, 136402.

Warren, J. L., Yarnell, J. L., Dolling, G. & Cowley, R. A. (1967). *Phys. Rev.* **158**, 805–808.

Watanabe, H., Shirakawa, T. & Yunoki, S. (2013). *Phys. Rev. Lett.* **110**, 027002.

Witczak-Krempa, W., Chen, G., Kim, Y. B. & Balents, L. (2014). *Annu. Rev. Condens. Matter Phys.* **5**, 57–82.

Yan, Y. J., Ren, M. Q., Xu, H. C., Xie, B. P., Tao, R., Choi, H. Y., Lee, N., Choi, Y. J., Zhang, T. & Feng, D. L. (2015). *Phys. Rev. X*, **5**, 041018.

Yang, Y., Wang, W.-S., Liu, J.-G., Chen, H., Dai, J.-H. & Wang, Q.-H. (2014). *Phys. Rev. B*, **89**, 094518.

Yoshida, M., Ishii, K., Jarrige, I., Watanuki, T., Kudo, K., Koike, Y., Kumagai, K., Hiraoka, N., Ishii, H., Tsuei, K.-D. & Mizuki, J. (2014). *J. Synchrotron Rad.* **21**, 131–135.